Supplementary information for Confinement of long-lived interlayer excitons in WS_2/WSe_2 heterostructures

Alejandro R.-P. Montblanch,[1,*] Dhiren M. Kara,[1,*] Ioannis Paradisanos,[2] Carola M. Purser,[1,2] Matthew S. G. Feuer,[1] Evgeny M. Alexeev,[2,1] Lucio Stefan,[1,3] Ying Qin,[4] Mark Blei,[4] Gang Wang,[2] Alisson R. Cadore,[2] Pawel Latawiec,[5] Marko Lončar,[5] Sefaattin Tongay,[4] Andrea C. Ferrari,[2,†] and Mete Atatüre[1,‡]

[1] *Cavendish Laboratory, University of Cambridge, 19 J. J. Thomson Ave., Cambridge, CB3 0HE, UK*

[2] *Cambridge Graphene Centre, University of Cambridge, 9 J. J. Thomson Ave., Cambridge, CB3 0FA, UK*

[3] *The Faraday Institution, Quad One, Becquerel Avenue, Harwell Campus, Didcot, OX11 0RA, UK*

[4] *School for Engineering of Matter, Transport and Energy, Arizona State University, Tempe, AZ, 85287, USA*

[5] *School of Engineering and Applied Science, Harvard University, Cambridge, MA, 02138, USA*

CONTENTS

Supplementary Note S1: Bulk crystals and monolayer structural characterization 2

Supplementary Note S2: Characterisation of WS_2/WSe_2 heterostructure device 3

Supplementary Note S3: Delocalised interlayer excitons 6

Supplementary Note S4: Statistics of confined interlayer excitons: power saturation and magnetic-field dependence 7

Supplementary Note S5: Reversibility of confined interlayer exciton emission peaks and temporal variation 10

Supplementary Note S6: Power dependence of delocalised interlayer-exciton lifetime 11

Supplementary Note S7: Spectrally selective lifetime measurements on a nanopillar 12

Supplementary Note S8: Temperature dependence of confined interlayer-exciton lifetime 14

Supplementary Note S9: Confined and delocalised excitons in device B 18

Supplementary Note S10: Effect of thermal cycling on device performance 22

Supplementary References 25

Supplementary Note S1: Bulk crystals and monolayer structural characterization

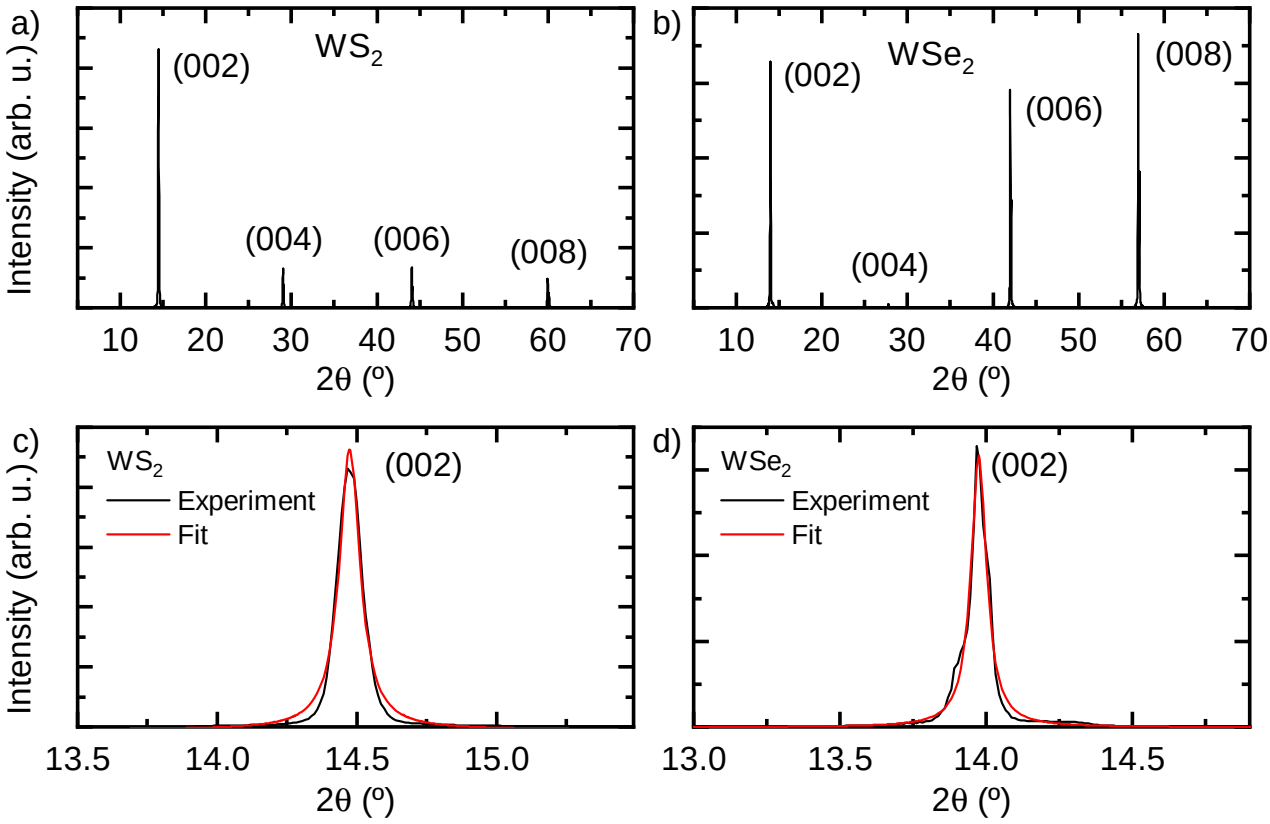

Supplementary Figure S1. **X-Ray Diffraction (XRD) of bulk WS_2 and WSe_2. (a)** XRD of bulk WS_2 at different angles with respect to the [001] crystal direction. **(b)** XRD of bulk WSe_2 at different angles with respect to the [001] crystal direction. **(c)** Black curve: (002) XRD peak of bulk WS_2 taken from (a). Red curve: Lorentzian fit to the experimental data. **(d)** Black curve: (002) XRD peak of bulk WSe_2 taken from (a). Red curve: Lorentzian fit to the experimental data.

To assess the presence of defects in the source crystals, we perform X-Ray Diffraction (XRD)[1] and Scanning Transmission Electron Microscopy (STEM)[2] measurements. These are in contrast to photoluminescence (PL) measurements performed on monolayers, which are dramatically influenced by factors unrelated to the crystal quality such as doping[3], electric fields[4], dielectric environment[5, 6], strain[7, 8], substrate[9, 10], or lack of hBN encapsulation[11].

In XRD, the intensity of X-ray photons directed at a bulk crystal is recorded for different impinging angles with respect to a given crystal plane. Intensity peaks arise for constructive interference across the atomic layers. The full-width at half maximum (FWHM) of the XRD peaks are a powerful tool to assess the crystallinity of the material[1]. The profile of the

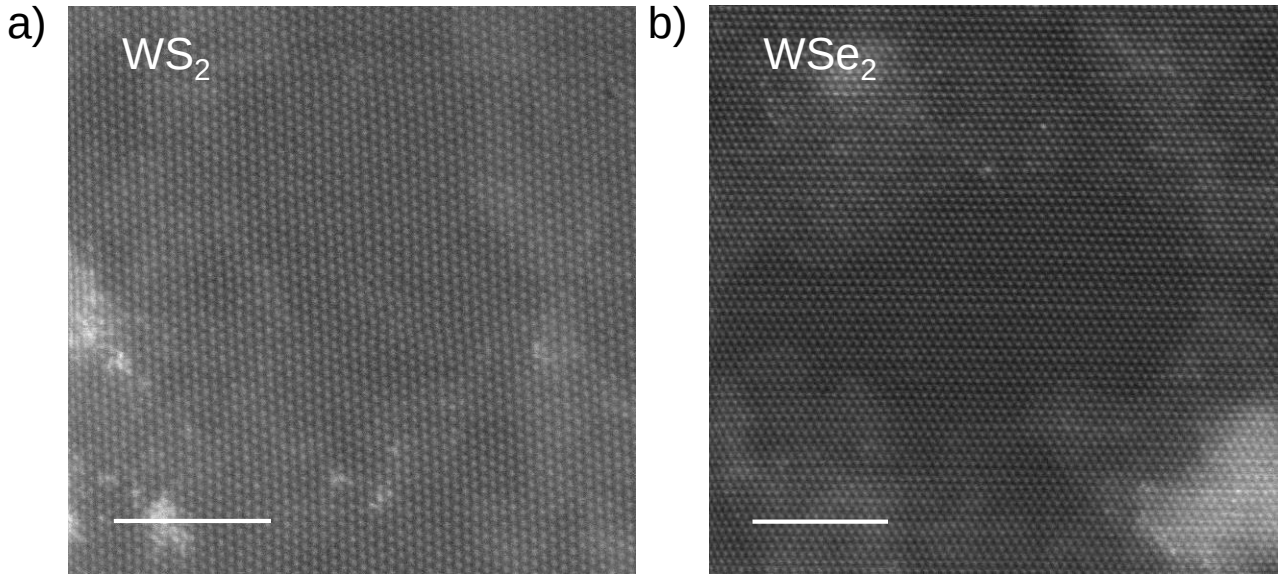

Supplementary Figure S2. **Scanning Transmission Electron Microscope (STEM) images of WS_2 and WSe_2 monolayers. (a)** STEM of monolayer WS_2. **(b)** STEM of monolayer WSe_2. Scale bars: 5 nm.

XRD peaks broadens with lattice spacing inhomogeneities caused by faulting, dislocations, and grain boundaries.

Supplementary Figures S1a,b are the XRD data of WS_2 and WSe_2 along the [001] crystal direction, respectively, collected with Panalytical Aeris. Lorentzian fittings of the (002) peaks (taken as representative peaks) of WS_2 and WSe_2 (Supplementary Figs. S1c,d) yield FWHM of $(0.0806\pm0.0016)^\circ$ and $(0.06434\pm0.0013)^\circ$. These are over a factor two better than the values reported in the literature[12, 13].

Supplementary Figures S2a and S2b are representative STEM images taken with JOEL 1200 EX TEM of WS_2 and WSe_2 monolayers mechanically exfoliated from bulk material and deposited on top of lacey carbon TEM grids. These give a point defect density $\sim 10^9$-10^{10} cm^{-2}, on par or better than the state of the art[14].

Supplementary Note S2: Characterisation of WS_2/WSe_2 heterostructure device

To characterise our devices structurally we perform room-temperature Raman measurements in a commercial Horiba LabRam Evolution system using a 514-nm laser at 60 µW. Supplementary Figure S3a shows the Raman spectrum from the WS_2/WSe_2 heterostructure (device A) on a flat region. The Raman peaks at $\sim$358 and $\sim$419 cm^{-1} correspond to the

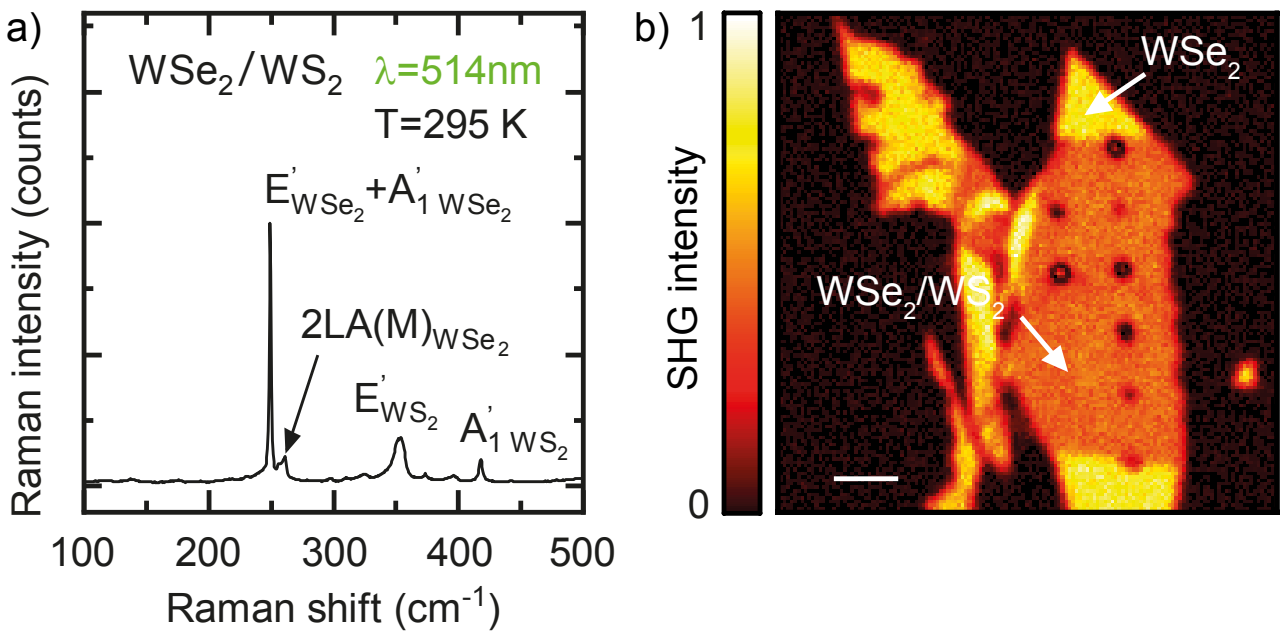

Supplementary Figure S3. **Raman and second harmonic signal of WS_2/WSe_2 heterostructure.** **(a)** Room-temperature Raman spectrum of WS_2/WSe_2 heterostructure. **(b)** Spatially resolved intensity of the second-harmonic signal of WS_2/WSe_2 heterostructure measured with 982-nm pump laser. Scale bar: 4 µm.

$E^{'}$ and $A_1^{'}$ modes of WS_2 monolayer, respectively [15]. The peak ∼251 cm^{-1}, with FWHM ∼2 cm^{-1}, is assigned to the convoluted $A_1^{'}$+$E^{'}$ modes of WSe_2, degenerate in monolayer WSe_2[15, 16], while the peak at ∼262 cm^{-1} belongs to the 2LA(M) mode of monolayer WSe_2[15].

The FWHM of ∼2 cm^{-1} of the convoluted $A_1^{'}$+$E^{'}$ modes of WSe_2 provides further evidence (see Supplementary Note S1) of the crystallinity of the material: it is consistent with that measured for devices that yielded PL spectra with extremely sharp excitonic lines[3]. For monolayer WS_2, the $A_1^{'}$ mode is symmetric in our device, in contrast to the expected asymmetry in the presence of defects[17].

Supplementary Figure S3b plots the spatially resolved map of the second-harmonic signal intensity from monolayer and heterostructure regions in device A. This is measured with a pulsed Ti:Sapphire laser (∼3-ps pulse duration) at 76 MHz repetition rate and tuned to 982 nm at ∼1 mW CW-equivalent power. From the reduced intensity in the heterostructure region compared to monolayer in Supplementary Fig. S3b we infer a stacking angle between WSe_2 and WS_2 monolayers of ∼50°, closer to 60° because the stacking of the individual constituents close to that angle yield partial destructive interference resulting from the

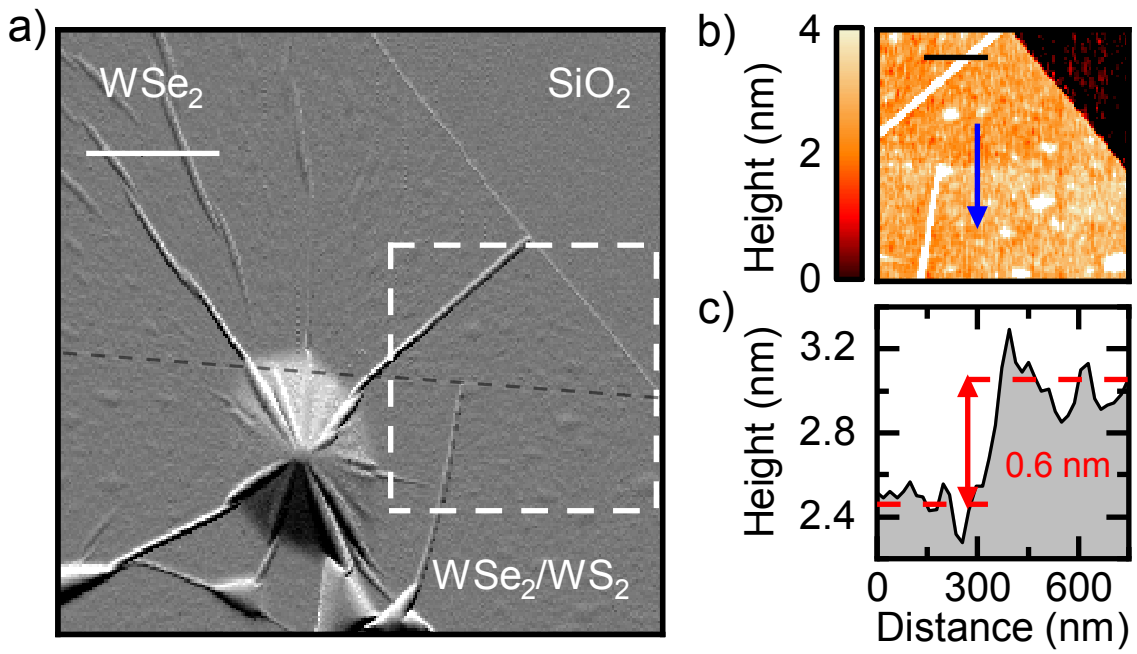

Supplementary Figure S4. **Atomic force microscope image of the heterostructure. (a)** Amplitude retrace of a device area with SiO_2, WSe_2 monolayer and WS_2/WSe_2 heterostructure regions. The black dashed line marks the boundary between the last two regions. Scale bar: 500 nm. **(b)** Topography of the area enclosed by the white dashed square in panel a. Scale bar: 500 nm. **(c)** Height profile obtained as the average height across the line cuts spanning a length of 350 nm centered around the blue arrow in panel b.

combination of the second harmonic signal from each individual monolayer[18]. This is confirmed by additional polarisation-resolved second-harmonic generation measurements at 1300-nm pump wavelength.

Supplementary Figure S4a is the map of the amplitude retrace in the room-temperature atomic force microscope measurement (MFP-3D from Asylum Research with silicon tips from Bruker) of an area of device A containing flat WSe_2 monolayer and WS_2/WSe_2 heterostructure regions, as well as WS_2/WSe_2 heterostructure on a nanopillar. We observe several wrinkles in the heterostructure when on a nanopillar, which might be the cause of multiple sharp emission peaks per nanopillar site. Control of quantum emitters could be achieved by using piezo-actuators[19, 20], nanopillars with different geometries[21], and taller nanopillars[22]. Supplementary Figure S4b shows the topography of the area enclosed by the white dashed square in Supplementary Fig. S4a. Supplementary Figure S4c plots the height profile obtained averaging the line cuts spanning a length of 350 nm centered around the blue arrow of Supplementary Fig. S4b. It shows that the step size from the WSe_2

monolayer region to the WS_2/WSe_2 heterostructure region coincides with the thickness of a monolayer, ∼0.6 nm[23].

Supplementary Note S3: Delocalised interlayer excitons

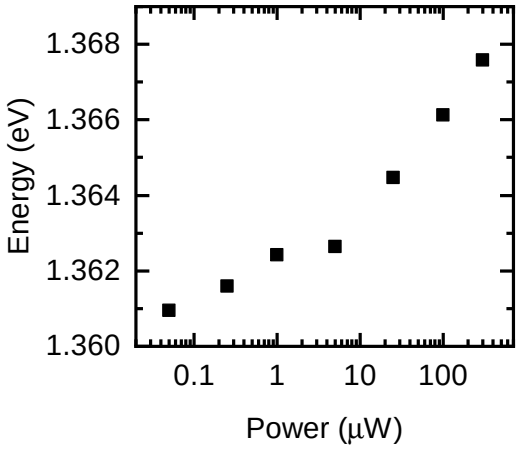

Supplementary Figure S5. **Power dependence of the energy of the delocalised interlayer exciton.** Weighted average of the energy of the delocalised interlayer exciton as a function of excitation power at 4 K.

We now explore the nature of the delocalised interlayer exciton emission that we present in Figs. 1d iii and 2a of the main text. Supplementary Figure S5 is the weighted average of the energy of the entire delocalised spectrum for different excitation powers, calculated as the sum of Intensity(E)×E divided by the total intensity for each spectrum, where E is the energy. We observe a blueshift by ∼7 meV over 4 orders of magnitude of laser excitation power, in agreement with Refs. [24, 25].

Supplementary Figure S6a is the PL spectra of the delocalised interlayer exciton at 4 K, 0-T magnetic field and four circular polarisation combinations in the excitation and detection paths, where light is right-circularly (σ^+) or left-circularly (σ^-) polarised. We do not observe a dependence of the intensity of σ^+ or σ^- emission on pump polarisation.

Supplementary Figure S6b is the PL spectrum of the delocalised interlayer exciton for magnetic fields of 8 T (black curve), 0 T (red curve) and -8 T (blue curve) under a $\sigma^+_{\mathrm{exc}}/\sigma^+_{\mathrm{det}}$ polarisation scheme, with the blue curve multiplied by a factor 20. This change in intensity indicates the strong thermalisation of delocalised interlayer excitons that results from band shifting under a magnetic field[3]. The non-uniform thermalisation across the

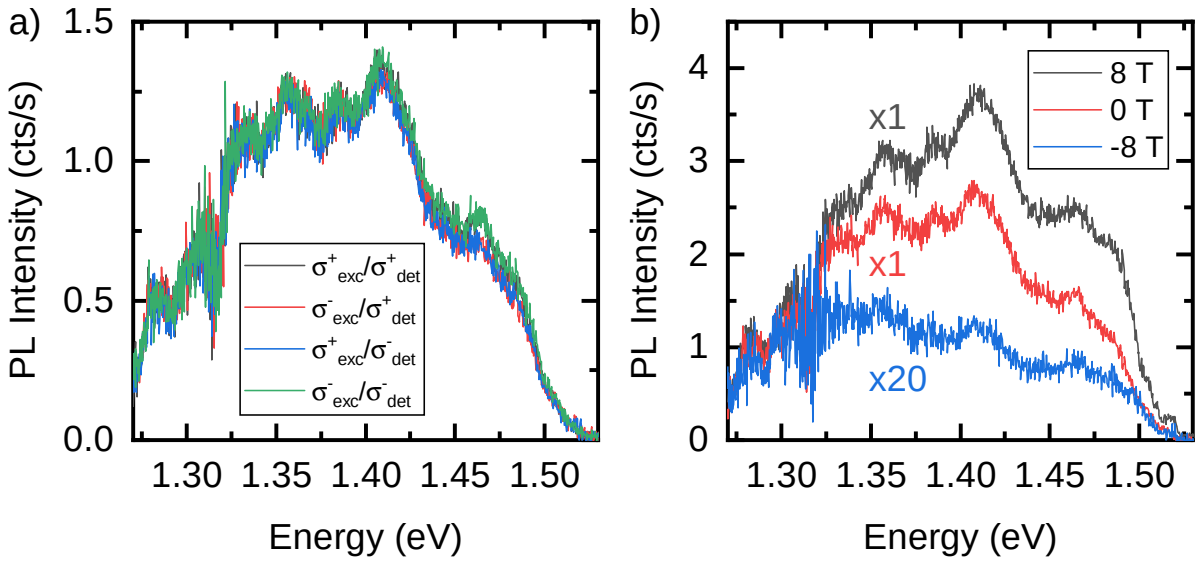

Supplementary Figure S6. **Polarisation and magnetic-field dependence of the delocalised interlayer exciton.** **(a)** Photoluminescence (PL) spectra at 4 K of the delocalised interlayer exciton at 0-T magnetic field and four different circular polarisation combinations. **(b)** PL spectra at 4 K of the delocalised interlayer exciton at 8-T (black), 0-T (red) and -8-T (blue) for a $\sigma^+_{\rm exc}/\sigma^+_{\rm det}$ polarisation combination. The numbers in black, red and blue indicate the factor by which the black, red and blue spectra have been multiplied, respectively.

spectrum combined with its broad width prevents reliable extraction of g-factors for the delocalised interlayer excitons. We attribute the broad emission to device inhomogeneity[26] and phonon-assisted processes[27]. For large twist-angles, transitions are not momentum-direct and emission occurs via phonon-assisted decay, which induces a broadening of the spectra[28].

Supplementary Note S4: Statistics of confined interlayer excitons: power saturation and magnetic-field dependence

In Ref. [22] we observed quantum confinement at two thirds of all nanopillar sites. Therefore, we expect a $\sim (2/3)^2$ success rate in our heterostructure devices. Indeed, we observe sharp emission lines from 8 of 16 nanopillar sites covered by the heterostructure in device A. We find on these 8 nanopillar sites an average of 15±6 sharp emission peaks (i.e. emission peaks with FWHM<2 meV), in the range between 1.34 eV and 1.45 eV, with saturating behaviour.

Supplementary Figure S7a are the same PL spectra from Fig. 2c in the main text. We

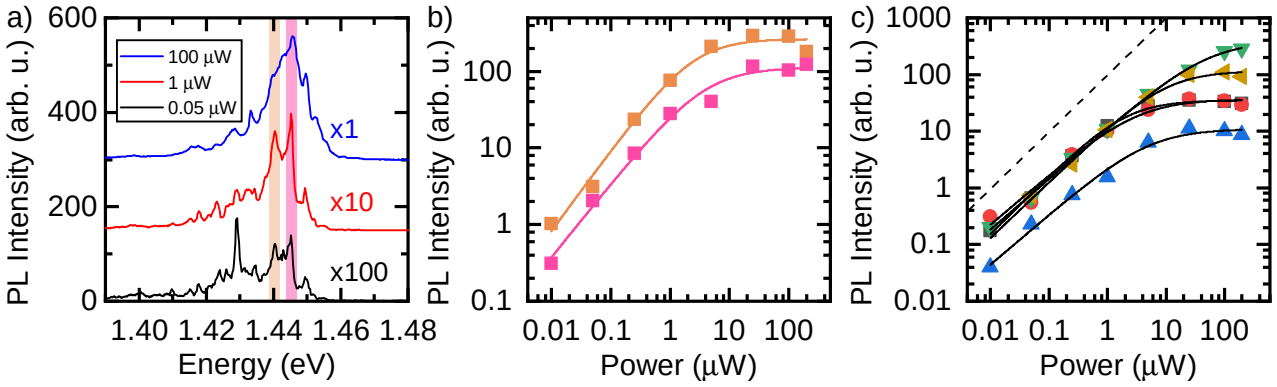

Supplementary Figure S7. **Saturation curves of confined interlayer excitons across different pillar locations. (a)** Photoluminescence (PL) spectra at 4 K of confined interlayer excitons on a nanopillar. This panel is the same as in Fig. 2c in the main text. **(b)** Orange and pink squares: integrated PL intensity as a function of continuous-wave excitation power of the confined interlayer exciton emission peaks highlighted in orange and pink in panel a, respectively. Orange and pink curves: saturation curve fits following Supplementary Eq. (1) of orange and pink data points, respectively. We fit n=0.96±0.08 and 1.05±0.09; and P_{sat}=3.6 and 2.5 μW for the pink and orange emission peaks, respectively. **(c)** Saturation curves under continuous-wave excitation of confined interlayer excitons across different nanopillar locations. The solid lines are fits using Supplementary Eq. (1), and the dotted line corresponds to a linear excitation power dependence. All fits present an initial linear dependence with excitation power P up a few μW, and then saturate.

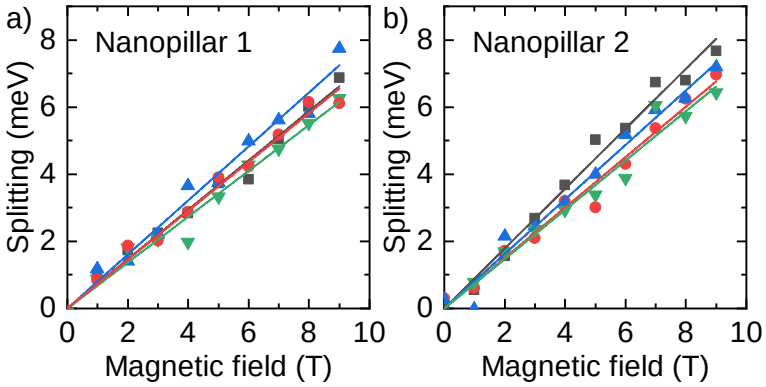

Supplementary Figure S8. **Zeeman splittings of confined interlayer excitons across different nanopillars**. Zeeman splitting of confined interlayer exciton emission on two nanopillars. Curves are linear fits to the Zeeman splittings, each corresponding to the various confined interlayer excitons within a given nanopillar location.

highlight two additional emission peaks in orange and pink, whose saturation curves we plot in Supplementary Fig. S7b. Supplementary Fig. S7c shows power saturation curves of confined interlayer excitons on different nanopillar locations at T=4 K, showing that the saturation behaviour of confined interlayer excitons is reproducibly found across the device. In Fig. 2d of the main text and Supplementary Figs. S7b and S7c of the SI we fit the

saturation data to the function

$$A \times P^n/(P_{\text{sat}} + P^n) \tag{1}$$

where P is the excitation power, A is the PL intensity at saturation, P_{sat} is the saturation power, and n is the exponent of the power law followed by P at low excitation powers.

We find a distribution of saturation powers P_{sat} with average 6 µW and standard deviation 3 µW, indicative of a range of slightly dissimilar confining potentials. This is supported by the observed variation in confined exciton g-factors and lifetimes (Figs. 3c and 4c in the main text). We find an average value of n=1.00±0.12. This linear dependence, reproduced across device A (and also in device B, see Supplementary Note S9), suggests that the confined interlayer excitons do not experience density-dependent decay mechanisms due to excitons around the nanopillar. This contrasts evidence of strong density dependence of the delocalised interlayer excitons, which exhibit non-linear excitation-power dependence (Fig. 2b in the main text) as well as population-dependent lifetimes (Supplementary Fig. S11). The number of sharp emission peaks and their statistical parameters regarding the power dependence apply as well to device B. We also note that the absence of higher power laws reveals that we are not losing excitons to the formation of multi-exciton species[25, 29].

Supplementary Figure S8 plots the Zeeman splitting of confined interlayer exciton emission in two example nanopillar locations. The solid curves are linear fits to the data, from which we extract the g-factors of the confined interlayer excitons according to[30]:

$$\Delta E = E_{\sigma_-} - E_{\sigma_+} = g\mu_{\text{B}}B \tag{2}$$

where E_{σ_+} (E_{σ_-}) is the emission energy of a confined interlayer exciton with σ_+ (σ_-) collection, g is the confined interlayer exciton g-factor, $\mu_{\text{B}} = 58$ µeVT^{-1} is Bohr's magneton and B is the applied magnetic field. The g-factors obtained from the linear fits in Supplementary Fig. S8b contribute to the Zeeman splitting distribution of similar g-factors with average value 13.2 and standard deviation 1.1, as stated in the main text and represented in Fig. 3c by a blue-shaded area. The similarity in the g-factor distribution between both locations suggests that the magnetic states at each confining potential have the same microscopic origins, albeit not identical across a given nanopillar location.

Supplementary Note S5: Reversibility of confined interlayer exciton emission peaks and temporal variation

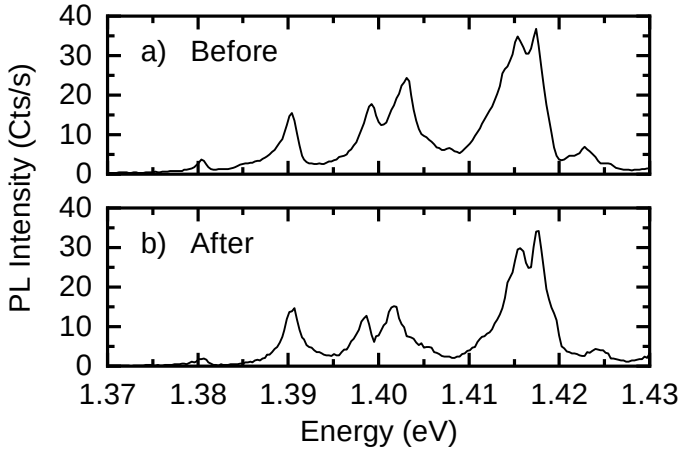

Supplementary Figure S9. **Photoluminescence spectra of confined interlayer excitons before and after a saturation series. (a)** Photoluminescence (PL) spectrum of confined interlayer excitons on a nanopillar before a saturation series. **(b)** PL spectrum of confined interlayer excitons on the same nanopillar as in panel a after a saturation series (up to 300μW excitation).

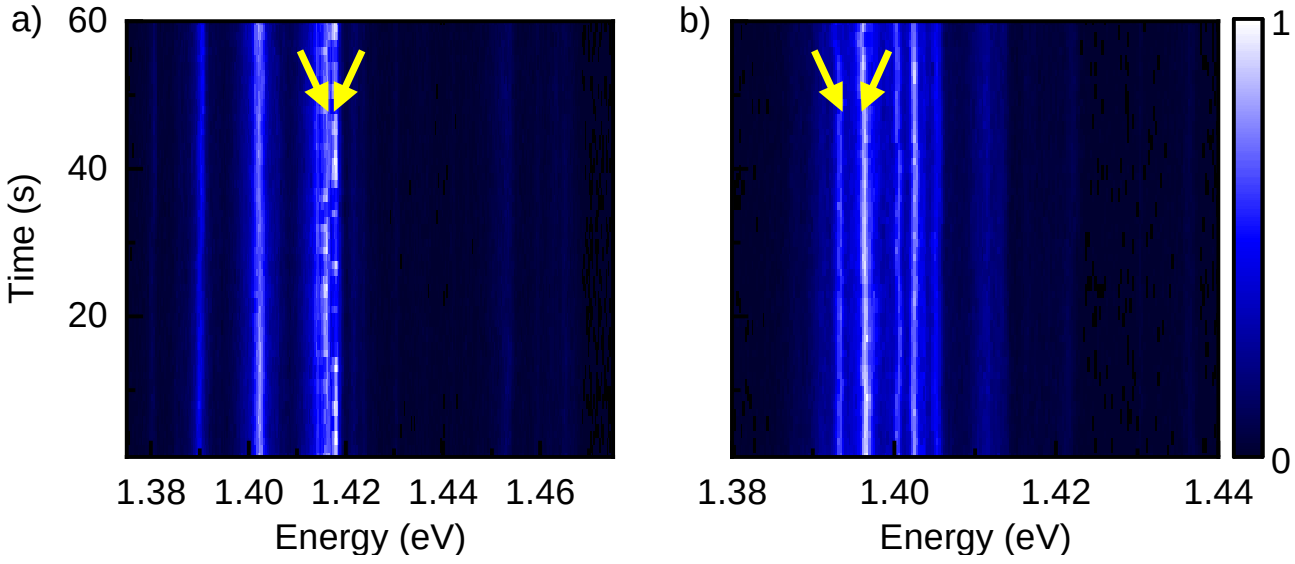

Supplementary Figure S10. **Time series of confined interlayer excitons. (a)** PL spectra taken once every second for 60 s on a nanopillar. **(b)** Same as in panel a, but on another nanopillar. In panels a and b the yellow arrows indicate the pair of emission peaks that exhibit anti-correlated intensity in time. Pearson's correlation coefficients are -0.88 and -0.73 for the pairs in panels a and b, respectively.

Supplementary Figures S9a,b are the PL spectra of confined interlayer excitons taken on a

nanopillar site before and after it is addressed with a maximum excitation power of 200 µW, respectively. We observe no drastic change in the shape of the PL from confined interlayer excitons, number of emission peaks, or energy position. This indicates that no photodoping, damage or non-reversible process is taking place in the device up to the maximum excitation power we used.

Supplementary Figures S10a,b are the PL spectra of confined interlayer excitons taken once every second for 60 s on two different nanopillars. We observe a robust emission in terms of energy, with the maximum observed variation in energy being ∼1 meV in 60 s. In terms of emission intensity, the majority fluctuate <20%. Some emission peak pairs display anti-correlated intensities, typical of confined systems with different charging environments or charged states[31, 32]. In Supplementary Figs. S10a,b, the pairs of emission peaks marked with yellow arrows exhibit this.

Supplementary Note S6: Power dependence of delocalised interlayer-exciton lifetime

We measure the lifetime of the delocalised interlayer excitons as a function of *average* pump power, $\bar{P}$, at T=4 K. We adjust $\bar{P}$ by gating the pulsed laser (76-MHz repetition rate/13-ns pulse separation) with varying gate windows from 50 ns up to 500 ns for a fixed histogram range of 1 ms. Supplementary Figure S11 are lifetime measurements for three $\bar{P}$ in the linear pump power-PL intensity regime: $\bar{P}$ = 2.5 nW (black filled circles), $\bar{P}$ = 7.5 nW (red filled circles) and $\bar{P}$ = 25 nW (blue filled circles). The two lifetimes τ_1 and τ_2 quoted in Supplementary Fig. S11 for each measurement are extracted from biexponential fits (solid curves). At larger pump powers a biexponential fit is required (see for example the red curve), while at lower pump powers a monoexponential fit suffices (as evidenced by the large fit error of the lifetime taken with the lowest $\bar{P}$ = 2.5 nW, black curve). This suggests a change in the dynamics of delocalised interlayer excitons with increasing $\bar{P}$. In the linear excitation power regime, where the intensity scales linearly with $\bar{P}$, we observe a variation of both τ_1 and τ_2. This contrasts the behaviour of a non-interacting system, where the measured lifetimes would remain constant. Thus, this measurement supports the existence of density-dependent dynamics of delocalised interlayer excitons, as discussed for Fig. 2c of the main text.

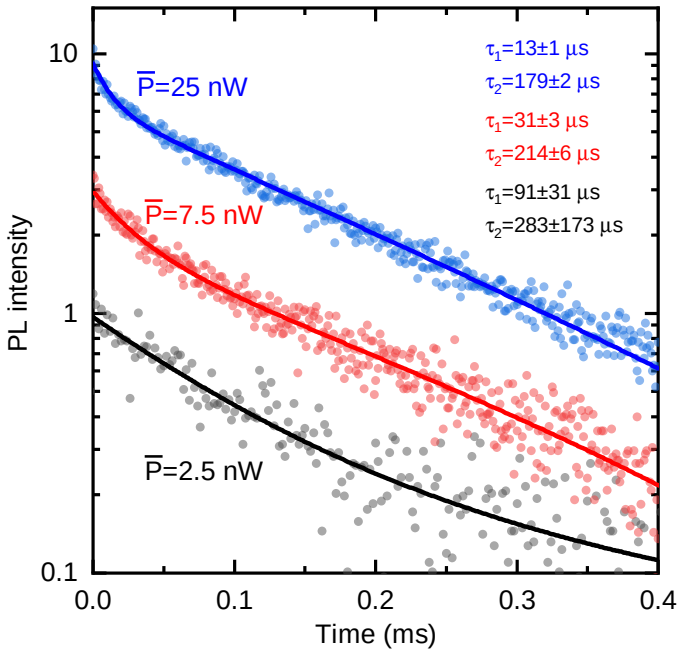

Supplementary Figure S11. **Lifetime of delocalised interlayer exciton for different average pump power.** The fluence equivalent is calculated by considering that 1 mW average power $\bar{P}$ (without down-sampling by the acousto-optical modulator, see Methods) corresponds to a fluence of $\sim$0.01 nJ·µm^{-2} per pulse. Filled circles are data points and solid lines are biexponential fits. Lifetimes τ_1 and τ_2 are extracted from the fits of the three measurements.

Supplementary Note S7: Spectrally selective lifetime measurements on a nanopillar

Supplementary Figure S12 is a lifetime measurement on a nanopillar at T=4 K: the red (blue) dots correspond to the red-shaded (blue-shaded) spectral region of the PL spectrum in the inset. The black dots are the lifetime measurement of the whole spectrum. All measurements are best fit with a biexponential function (solid curves in Supplementary Fig. S12), from which we extract τ_s =24.2±4.0 ns and τ_l =3.53±0.09 µs (red), τ_s =104.6 ±2.7ns and τ_l =1.66±0.03 µs (blue), and τ_s =159.9±8.8 ns and τ_l =3.00±0.10 µs (black). Thus, the biexponential behaviour is maintained regardless of the selected spectral window, and is observed across all nanopillar locations.

While there is a slight variation, expected for distinct confining potentials across a nanopillar, lifetimes are within the same order of magnitude for different spectral regions and we do not capture any correlation between spectrum and lifetime. The biexponential is observed down to the single-emission-peak level, as presented in the lifetime measurement in Fig. 4b of the spectrally isolated emission peak at 1.39 eV in Fig. 3d of the main text.

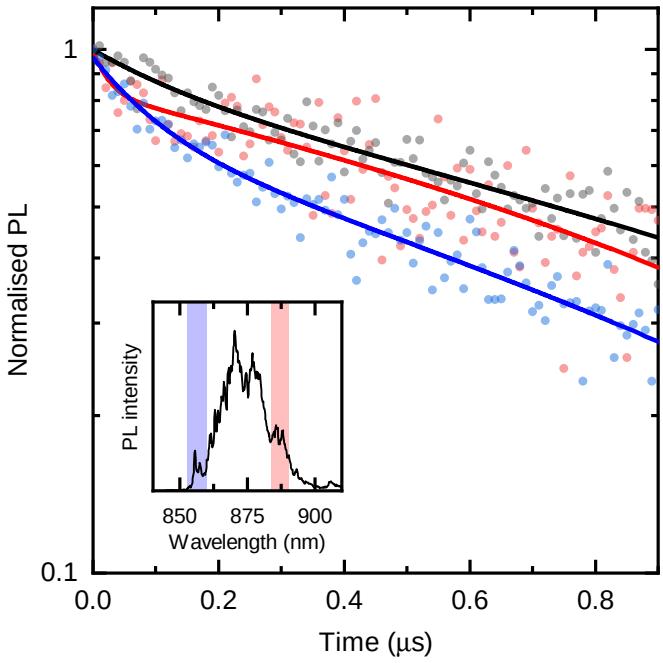

Supplementary Figure S12. **Lifetime measurement of three spectral regions of the photoluminescence signal on a nanopillar.** Dots are data and solid lines are biexponential fits. Lifetimes in red and blue correspond to the spectral regions shaded in red and blue, respectively, in the photoluminescence (PL) spectrum in the inset. The lifetime of the whole PL spectrum in the inset is in black.

The similarity between the lifetime of the spectrally selected regions and the lifetime extracted for the integrated PL spectrum, combined with the similarity in intensities among all emission peaks for a given nanopillar, prevents the distinction of each individual biexponential decay for each single emission peak in a lifetime measurement of the integrated PL spectrum on a nanopillar. The measured lifetimes are thus representative of the average lifetimes for confined interlayer excitons at each nanopillar, and justifies our reporting of the average lifetime from each nanopillar in Fig. 4c as extracted by collecting the PL from the entire, integrated PL spectrum. The absence of timescales on the order of hundreds of μs in the lifetimes of confined interlayer excitons indicates that funnelling[33] does not play a significant role in their recombination process.

Supplementary Note S8: Temperature dependence of confined interlayer-exciton lifetime

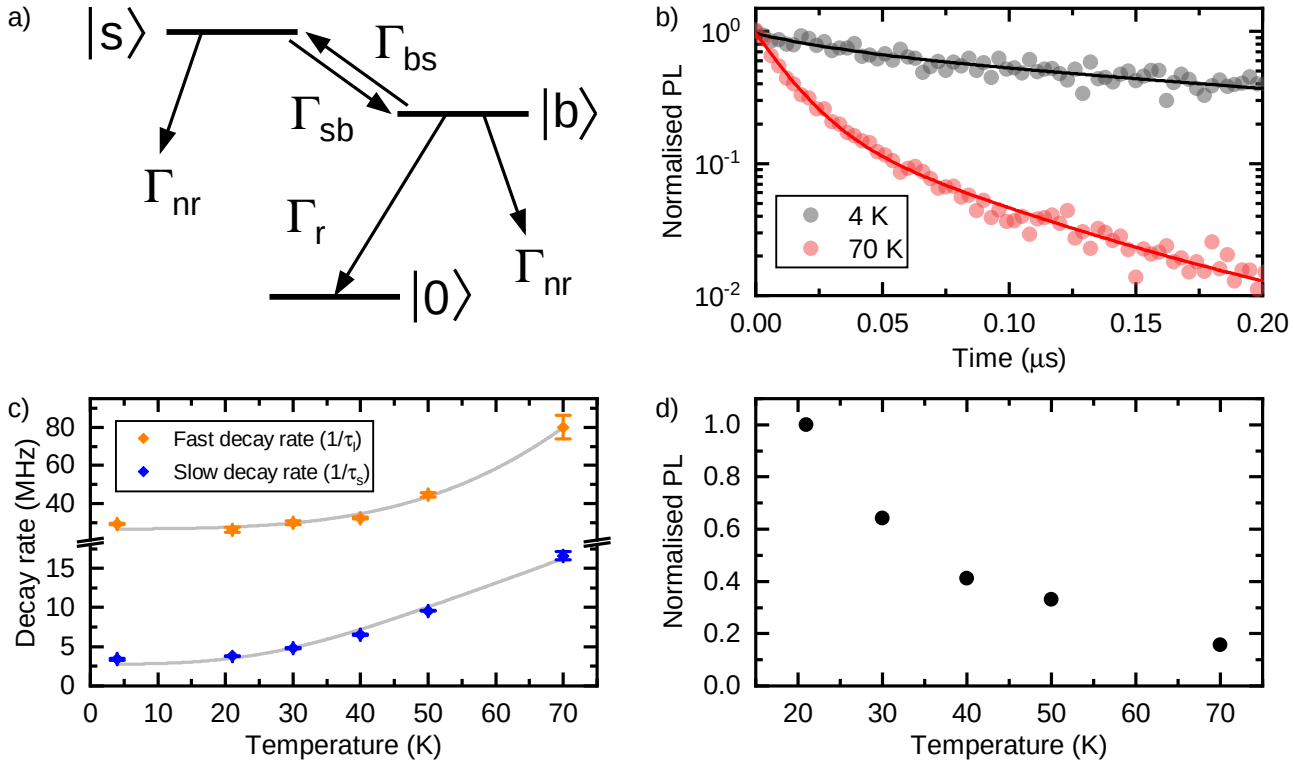

Supplementary Figure S13. **Three-level model and lifetimes of confined interlayer excitons as a function of temperature**. **(a)** Schematic representation of the three-level model used to explain the biexponential behaviour of confined interlayer excitons. The meaning of each rate is specified in the text. **(b)** Lifetime measurement of an example confined interlayer exciton at 4 K (black dots) and 70 K (red dots). The black and red curves are biexponential fits to the data at 4 K and 70 K, respectively. **(c)** Decay rates as a function of temperature obtained from biexponential fits to lifetime measurements on an example confined interlayer exciton. The fast (slow) decay rate $1/\tau_s$ ($1/\tau_l$) is represented by orange (blue) diamonds. Error bars are obtained from the fitting errors of the lifetime measurements. The solid grey curves are theoretical fits obtained using the model described in the text. **(d)** Photoluminescence intensity on a nanopillar-confined interlayer exciton as a function of temperature.

To explain the biexponential decay of the confined interlayer excitons we consider a three-level model, depicted in Supplementary Fig. S13a, consisting of a bright state $|b\rangle$, an optically inactive shelving state $|s\rangle$ and a ground state $|0\rangle$. Similar models were used in other systems with biexponential decay characteristics, such as self-assembled quantum dots[34] and carbon nanotubes[35].

Following our discussion from the main text and Supplementary Note S4 regarding the

energy dependence of the confined interlayer excitons with an external magnetic field, we infer that the recombination of confined interlayer excitons is heavily influenced by the $K^{'}$-K transition[36, 37]. There are then two likely possibilities for the shelving state, where with respect to the bright exciton, the electron of the shelving state resides in the opposite spin state of the same valley, which is higher in energy for our closer to 60° aligned hetrostructure, or in the same spin state but in the opposite valley at the same energy (assuming that spin-exchange interactions are negligible for spatially separated electron and hole pairs). Our temperature-dependent lifetime measurements support the shelving state being higher in energy than the bright state as we explain below.

The rate equations governing the populations ρ_{b} and ρ_{s} of the bright and shelving states in such a system are:

$$\frac{\partial \rho_{\mathrm{b}}}{\partial t} = -(\Gamma_{\mathrm{r}} + \Gamma_{\mathrm{nr}} + \Gamma_{\mathrm{bs}})\rho_{\mathrm{b}} + (\Gamma_{\mathrm{sb}})\rho_{\mathrm{s}} \tag{3}$$

$$\frac{\partial \rho_{\mathrm{s}}}{\partial t} = -(\Gamma_{\mathrm{nr}} + \Gamma_{\mathrm{sb}})\rho_{\mathrm{s}} + (\Gamma_{\mathrm{bs}})\rho_{\mathrm{b}} \tag{4}$$

where the radiative rate for the bright state is Γ_{r}, the coupling rates between the bright and the shelving states are Γ_{bs} (bright to shelving) and Γ_{sb} (shelving to bright), and the nonradiative decay rate for the bright and shelving states (assumed to be equal) is Γ_{nr}.

Solving Supplementary Eqs. (3,4) yields a biexponential population decay in time for $\rho_{\mathrm{b}}(t)$ of the form $\mathrm{A_s e^{-t/\tau_s}} + \mathrm{A_l e^{-t/\tau_l}}$ as written in the main text, with time constants given by

$$\frac{\Gamma_{\mathrm{r}} + \Gamma_{\mathrm{bs}} + \Gamma_{\mathrm{sb}}}{2} + \Gamma_{\mathrm{nr}} \pm \sqrt{\left(\frac{\Gamma_{\mathrm{r}} + \Gamma_{\mathrm{bs}} - \Gamma_{\mathrm{sb}}}{2}\right)^2 + \left(\frac{\Gamma_{\mathrm{bs}} + \Gamma_{\mathrm{sb}}}{2}\right)^2 - \left(\frac{\Gamma_{\mathrm{bs}} - \Gamma_{\mathrm{sb}}}{2}\right)^2}. \tag{5}$$

We identify the fast decay rate $\Gamma_{\mathrm{s}} = \frac{1}{\tau_{\mathrm{s}}}$ with the + sign of Supplementary Eq. (5) and the slow decay rate $\Gamma_{\mathrm{l}} = \frac{1}{\tau_{\mathrm{l}}}$ with the - sign of Supplementary Eq. (5).

We perform temperature-dependent lifetime measurements to elucidate the dominating rate and gain insight on the decay mechanisms. Supplementary Figure S13b is an example lifetime measurements taken on a nanopillar at 4 K (black filled circles) and 70 K (red filled circles). We extract, for an example nanopillar location, the two exponents of the biexponential fit at different temperatures, and present them as rates $1/\tau_{\mathrm{s}}$ (fast decay rate)

and $1/\tau_{\rm l}$ (slow decay rate) in Supplementary Fig. S13b as orange and black dots, respectively. We observe a strong dependence of both $1/\tau_{\rm s}$ and $1/\tau_{\rm l}$ with temperature, suggesting that $\Gamma_{\rm nr}$, $\Gamma_{\rm bs}$ and $\Gamma_{\rm sb}$ (Fig. 4 in the main text) are thermally activated: a common mechanism for nonradiative processes, as well as coupling between a bright and a shelving state, is through phonon mediation. To model this coupling we assume a multi-phonon process involving a continuum phonon density of states[38] and set the temperature dependences for $\Gamma_{\rm nr}$, $\Gamma_{\rm bs}$ and $\Gamma_{\rm sb}$ to be, respectively:

$$\Gamma_{\rm nr}(T) = \gamma_{\rm nr}\left(1 + \alpha T^m\right) \tag{6}$$

$$\Gamma_{\rm sb}(T) = \gamma_{\rm sb}\left(1 + \beta T^m\right) \tag{7}$$

$$\Gamma_{\rm bs}(T) = \gamma_{\rm sb}\beta T^m \tag{8}$$

where T is temperature, $\gamma_{\rm nr}$ is the spontaneous non-radiative rate at 0 K, α is the pre-factor of T^m for $\Gamma_{\rm nr}$, $\gamma_{\rm sb}$ is the rate of population transfer from the shelved to the bright state at 0 K, β is the pre-factor of T^m for both $\Gamma_{\rm bs}$ and $\Gamma_{\rm sb}$, and m describes the power law scaling of $\Gamma_{\rm nr,bs,sb}$ with T. m depends on the exact phononic coupling mechanism[38], and we assume for simplicity to be the same for all $\Gamma_{\rm nr,bs,sb}$. The solid curves in Supplementary Fig. S13b are fits to the data obtained by substituting Supplementary Eqs. (6-8) into Supplementary Eq. (5), where $\Gamma_{\rm r}$ is left as a constant in T because it physically depends only on the optical dipole transition strength. We obtain $m \approx 3$, similar to that previously reported in other quantum emitters[38], and confirms the strong temperature dependence of $\Gamma_{\rm nr}$, $\Gamma_{\rm bs}$ and $\Gamma_{\rm sb}$. The remaining fit values are: $\Gamma_{\rm r} = 26.7 \pm 5.0$ MHz, $\gamma_{\rm nr} = 0.003 \pm 5.5$ MHz, $\alpha = 0.005 \pm 8.2$ K^{-3}, $\gamma_{\rm sb} = 2.7 \pm 6.0$ MHz and $\beta = (3.0 \pm 7.0) \times 10^{-5}$ K^{-3}.

With these values, $\Gamma_{\rm bs}$ contributes starting at $\sim$20 K, which corresponds to an energy of $\sim$2 meV, and $\Gamma_{\rm bs}$ becomes comparable in magnitude to $\Gamma_{\rm sb}$ at $\sim$40 K. Our model reveals that at low temperatures (below 20 K), when $\Gamma_{\rm bs}$ is small, Supplementary Eq. (5) can be approximated as:

$$\Gamma_{\rm l} \sim \Gamma_{\rm nr} + \Gamma_{\rm sb} \tag{9}$$

$$\Gamma_{\mathrm{s}} \sim \Gamma_{\mathrm{r}} + \Gamma_{\mathrm{nr}}. \tag{10}$$

From Fig. 4c of the main text we extract average values $1/\tau_{\mathrm{s}} = \Gamma_{\mathrm{s}}$=13 MHz and $1/\tau_{\mathrm{l}} = \Gamma_{\mathrm{l}}$=500 kHz. Since Γ_{nr} is present in both Supplementary Eqs. (9) and (10), we conclude that Γ_{s} in the biexponential fit of a lifetime measurement is a direct measure of Γ_{r} in the limit of low temperature, i.e. $\Gamma_{\mathrm{s}} \approx \Gamma_{\mathrm{r}}$ at 4 K. Hence, the dynamics of confined interlayer excitons is not limited by non-radiative processes. In particular, applying the fit parameters in Supplementary Eqs. (6-8) we obtain, for the nanopillar data in Supplementary Fig. S13c and at 4 K, Γ_{r}=26.7 MHz, Γ_{nr}=4 kHz and Γ_{sb}=2.7 MHz, so that Γ_{r} is at least one order of magnitude larger than Γ_{bs} or Γ_{nr}. The long-lived shelving state enables this relation: a model with only one excited state would yield a single exponential and not two. Additionally, the measured lifetimes up to 4 µs (Fig. 4c in the main text) indicate that a significant fraction of the confined interlayer excitons will live for that long, regardless of the mechanism.

At temperatures $\gtrsim$40 K, when $\Gamma_{\mathrm{bs}} \approx \Gamma_{\mathrm{sb}}$, the model becomes:

$$\Gamma_{\mathrm{s}} \sim \frac{\Gamma_{\mathrm{r}}}{2} + \Gamma_{\mathrm{sb}} + \Gamma_{\mathrm{nr}} + \sqrt{\left(\frac{\Gamma_{\mathrm{r}}}{2}\right)^2 + (\Gamma_{\mathrm{sb}})^2} \tag{11}$$

$$\Gamma_{\mathrm{l}} \sim \frac{\Gamma_{\mathrm{r}}}{2} + \Gamma_{\mathrm{sb}} + \Gamma_{\mathrm{nr}} - \sqrt{\left(\frac{\Gamma_{\mathrm{r}}}{2}\right)^2 + (\Gamma_{\mathrm{sb}})^2}. \tag{12}$$

With our fit parameters we find, at 70 K, Γ_{r}=26.7 MHz, Γ_{nr}=5.1 MHz, Γ_{sb}=30.5 MHz and Γ_{bs}=27.8 MHz, so that nonradiative processes and population transfer to the shelving state are at this temperature more relevant. Our model, where the shelving state is higher in energy than the bright state, predicts the decrease in quantum efficiency with increasing temperature. Indeed, the thermally induced modification in the dynamics is evidenced in Supplementary Fig. S13d: it plots the PL intensity of confined interlayer excitons as a function of temperature showing that, as nonradiative processes are thermally activated and population transfer rate to the shelving state increases, the PL intensity decreases.

Finally, we note that an exponential temperature dependence of the form $\exp\left(-\frac{E_{\mathrm{a}}}{k_{\mathrm{B}}T}\right)$ (with E_{a} the activation energy, k_{B} the Boltzmann constant and T temperature), used in other systems in the context of the Mott-Seitz model[39], also fits our data with similar parameter values. Thus, while the three-level model with temperature-dependent rates captures the

confined interlayer exciton dynamics, a thorough theoretical study and further experimental analysis is necessary to understand the full microscopic nature of the system.

Supplementary Note S9: Confined and delocalised excitons in device B

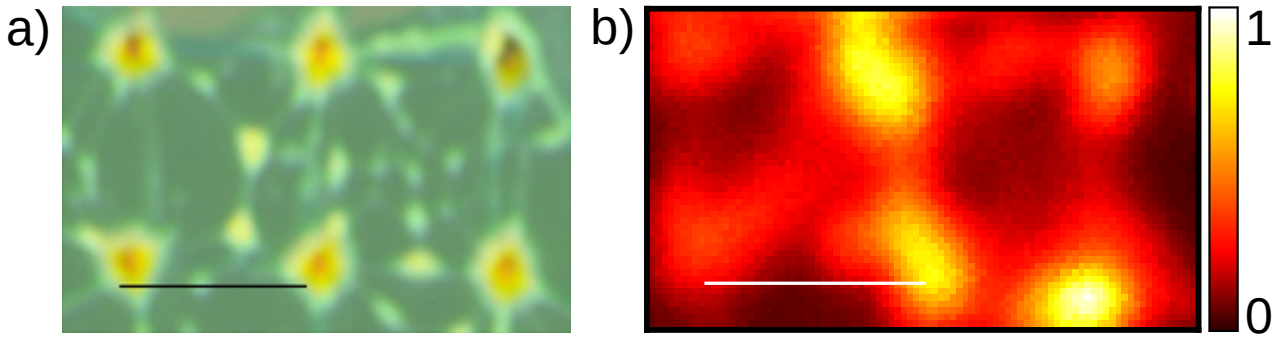

Supplementary Figure S14. **Optical image and photoluminescence intensity map of device B, WS_2/WSe_2 heterostructure on a nanopillared substrate. (a)** Optical image of the region of interest of device B. Scale bar: 4 µm. **(b)** Photoluminescence intensity map at 4 K of the region shown in panel a. Scale bar: 4 µm.

The reproducibility of our results is also verified on an additional WS_2/WSe_2 heterostructure on a nanopillar substrate, device B. The fabrication procedure as well as the source crystal are the same as device A. The only parameter changed is the alignment between the two monolayers, which in this case is $<7^\circ$ with respect to a high symmetry alignment as inferred from optical microscope images. This is a smaller misalignment compared to device A.

Supplementary Figure S14a is the optical image of a region of interest of device B, containing six nanopillars with a WS_2/WSe_2 heterostructure on top. Supplementary Figure S14b is the integrated PL map at 4 K in the same region as Supplementary Fig. S14a, evidencing that higher PL intensity is obtained on top of nanopillars. This is the same observation as in Fig. 1e of the main text. In device B, we observed sharp emission lines on 6 of the 10 addressed nanopillars.

Supplementary Figure S15a is a representative PL spectrum at 4 K obtained for above-bandgap CW excitation at 2.33 eV. Consequently, emission is observed from intralayer exciton emission from both WS_2 (green shading in Supplementary Fig. S15a) and WSe_2 (red shading in Supplementary Fig. S15a) monolayers, as well as interlayer exciton emission

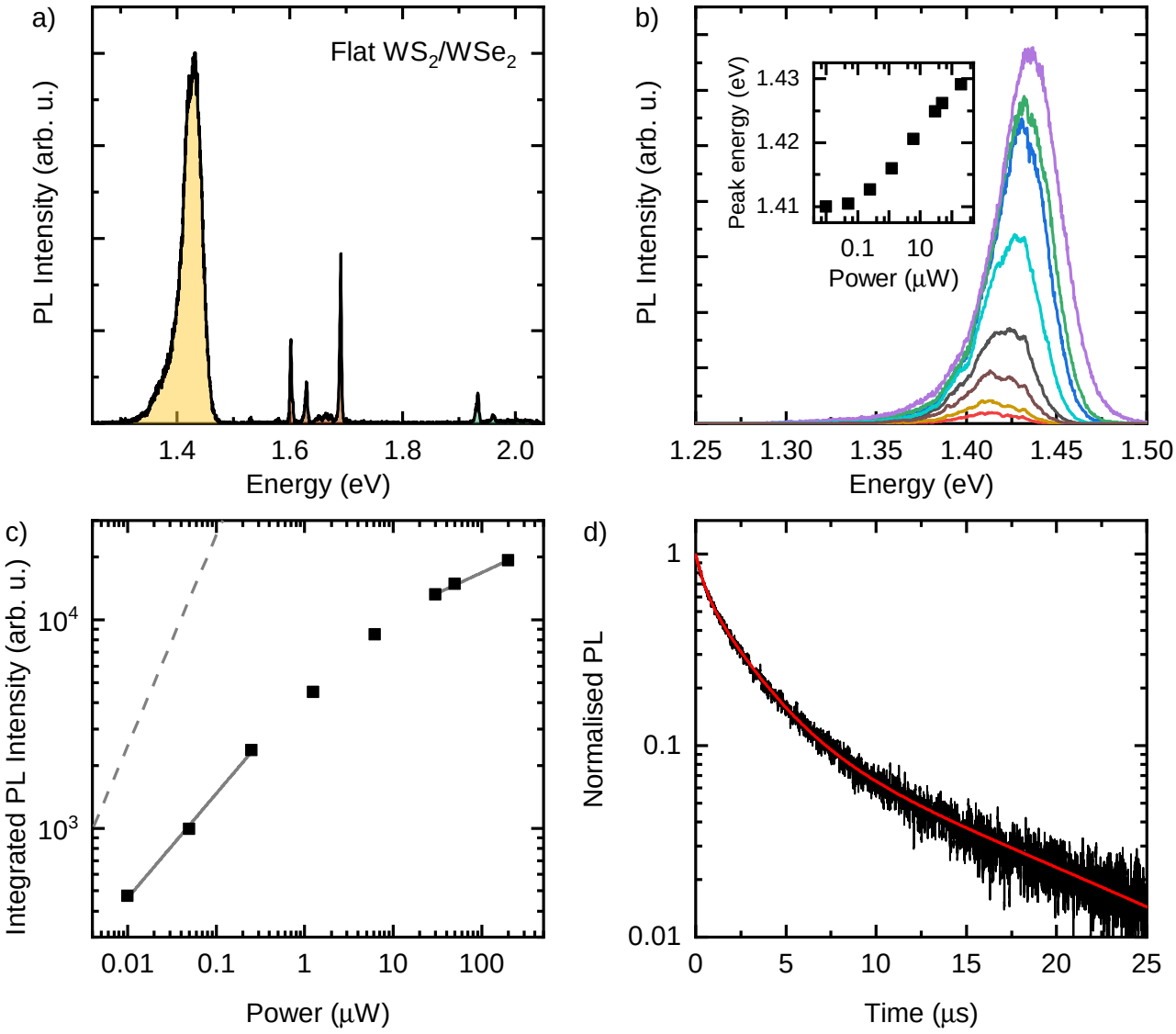

Supplementary Figure S15. **Photoluminescence properties at 4 K of delocalised interlayer excitons in device B. (a)** Representative photoluminescence (PL) spectrum under 2.33 eV continuous-wave (CW) excitation taken at a flat WS_2/WSe_2 heterostructure location. The colour coding indicates the origin of PL emission, where green (red) comes from intralayer excitons in WS_2 monolayer (WSe_2 monolayer), and yellow from interlayer excitons in WS_2/WSe_2 heterostructure. **(b)** PL spectra of delocalised interlayer exciton at different excitation powers. Inset: centre-of-mass energy of spectra shown in the main panel as a function of excitation power. **(c)** PL intensity of delocalised interlayer exciton as a function of excitation power, exhibiting sublinear power dependence. The two solid lines correspond to slopes 0.5 and 0.2. Dashed line: reference linear power dependence. **(d)** Lifetime of delocalised interlayer exciton under 1.50 eV pulsed excitation. Lifetime constants are 440 ns, 2.4 µs and 11.7 µs.

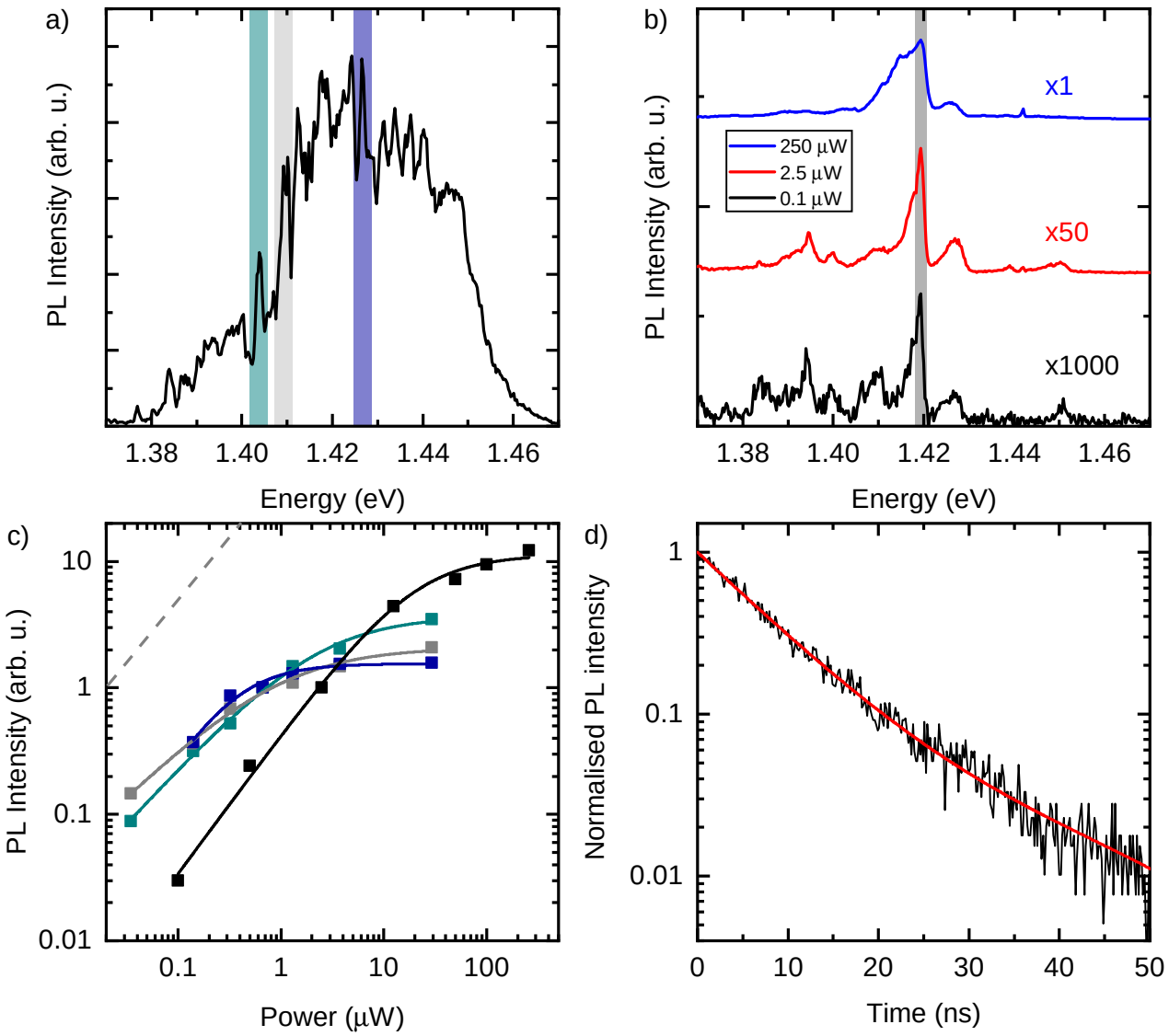

Supplementary Figure S16. **Photoluminescence properties at 4 K of confined interlayer excitons in device B. (a)** Example photoluminescence (PL) spectrum of WS_2/WSe_2 heterostructure on top of a nanopillar. **(b)** PL spectra from WS_2/WSe_2 heterostructure on a nanopillar at 0.01 (black), 2.5 (red) and 250-µW (blue) excitation. **(c)** Spectrally integrated PL intensity of the emission peaks shaded with green, grey and blue bands in panel a and in black in panel b as a function of P. Data (filled squares) are colour-coded to the spectral bands of panels a and b. Solid curves are fits using Supplementary Eq. (1). **(d)** Lifetime of confined excitons on a nanopillar. Time constants are 8 ns and 155 ns.

(yellow shading in Supplementary Fig. S15c). The width of the delocalised interlayer exciton emission in device B is less than half of that measured in device A, possibly due to a reduction in the roles played by phonon assisted processes and indirect transitions[27, 28] stemming from a smaller angle misalignment in device B.

Supplementary Figure S15b plots the PL spectra of the delocalised interlayer exciton obtained at different excitation powers. We extract a maximum blueshift of ∼20 meV at 200 µW as presented in the inset of Supplementary Fig. S15b. This is in agreement with Refs. [24, 25]. We extract and show in Supplementary Fig. S15c a sublinear dependence of PL intensity with excitation power P growing as $P^{0.5}$ initially and then as $P^{0.2}$ for higher powers. The observation of a sublinear dependence and a change in slope for higher powers is in agreement with Ref. [25], as well as Fig. 2b of the main text. Supplementary Fig. S15d is an example lifetime measurement of delocalised interlayer excitons at 4 K for 1.50-eV pulsed excitation, replicating the conditions for Fig. 4 in the main text. We obtain three time constants, whose averages over different locations on the flat WSe_2/WS_2 heterostructure are 440±190 ns, 2.6±0.2 µs and 10±2 µs. The long timescale of 10 µs is longer (by at least one order of magnitude) than what is typically observed in interlayer excitons. This lifetime is shorter than that in the main text (approaching 0.2 ms), which we ascribe to the smaller angle mismatch in device B.

Supplementary Figure S16a is an example PL spectrum at 4 K on a nanopillar, exhibiting several sharp (FWHM<2 meV) emission peaks. The energy spread of the sharp emission peaks in device B is approximately the same as for device A. Supplementary Fig. S16b plots an example spectrum on a nanopillar for different excitation powers: P=0.1 µW (black curve), 2.5 µW (red curve) and 250 µW (blue curve). Unlike for the delocalised interlayer exciton, we do not observe any blueshift, in accordance with the interpretation of these excitons being spatially isolated. This is the representative behaviour found across all confined interlayer excitons in this device, as well as device A. With increasing power, the sharp emission peaks in Supplementary Figs. S16a,b saturate. In Supplementary Fig. S16c we show the integrated PL intensity of the emission peaks highlighted in green, grey and blue from Supplementary Fig. S16a, as well as the emission peak highlighted in black from Supplementary Fig. S16b. They exemplify the saturation behaviour of the sharp interlayer exciton emission peaks on top of nanopillars. We fit the data according to Supplementary Eq. (1) and obtain an average slope of n=1.02 and a saturation power of P_{sat}=7.4 µW, in good agreement with the data we show in the main text. The initial linear power dependence of the confined interlayer excitons strongly contrasts the delocalised interlayer excitons (see Supplementary Fig. S16c). Supplementary Figure S16d is the lifetime measurement on top of a nanopillar at 4 K and 1.50 eV (same conditions as in the main text), from where we

extract two timescales: τ_s =8 ns and τ_l =155 ns, considerably shorter than the timescales of the delocalised counterpart, in agreement with the main text. In both the confined and delocalised cases, the presence of long timescales indicates that the recombination mechanism of interlayer excitons is not limited by non-radiative processes.

Supplementary Note S10: Effect of thermal cycling on device performance

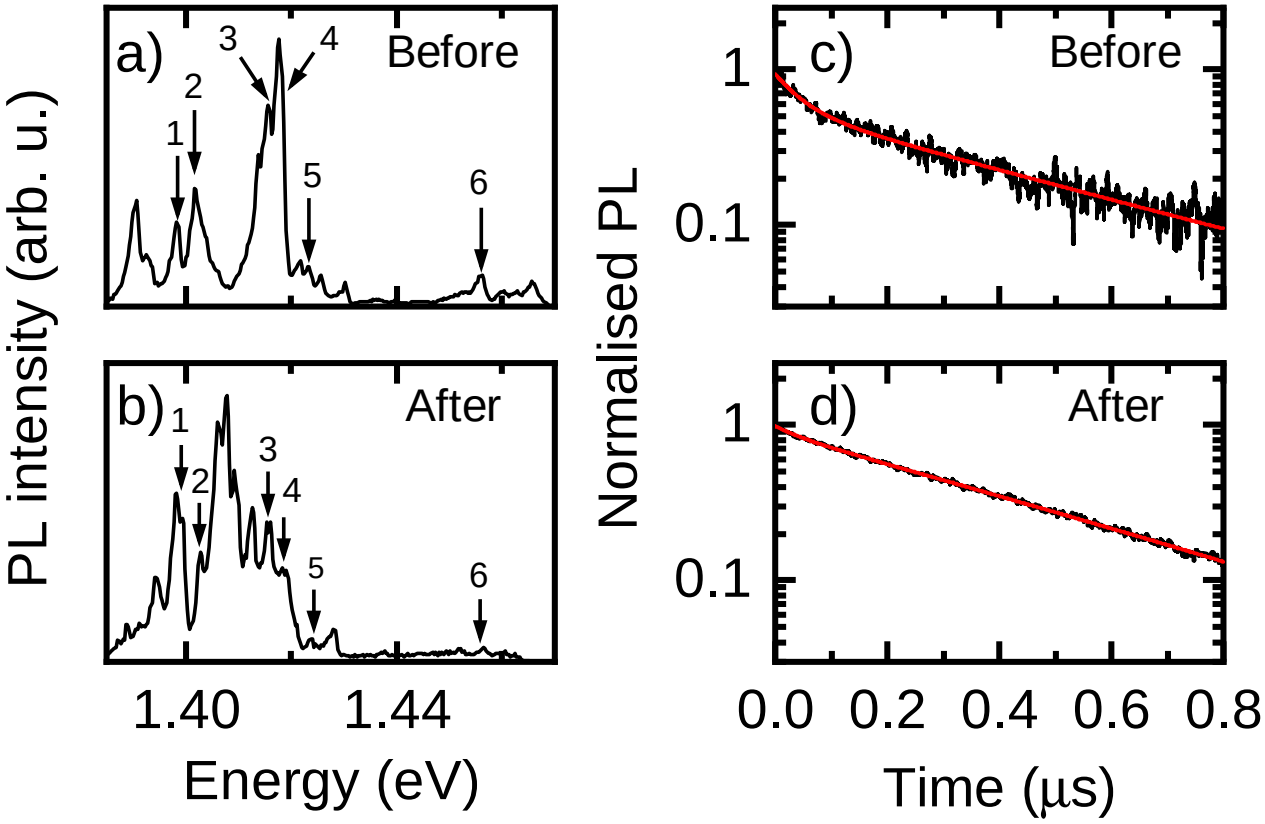

Supplementary Figure S17. **Effect of thermal cycling on the photoluminescence properties of confined interlayer excitons**. **(a)** Photoluminescence (PL) spectrum of confined interlayer excitons on a nanopillar at 4 K before the device is subjected to an additional warm-up, cool-down cycle. **(b)** PL spectrum on the same location as in panel a, at 4 K, after an additional warm-up, cool-down cycle. In both panels a and b, the numbers 1-6 correspond to confined interlayer exciton emission peaks which have likely survived the cycle, as identified by their spectral position. **(c)** Lifetime of the confined interlayer excitons from the spectrum in panel a, i.e. before the additional warm-up, cool-down cycle. The fit decay times from the biexponential are τ_s=45 ns and τ_l=430 ns. **(d)** Lifetime of the confined interlayer excitons from the spectrum in panel b, i.e. after the additional warm-up, cool-down cycle. The fit decay times from the biexponential are the same as in panel c.

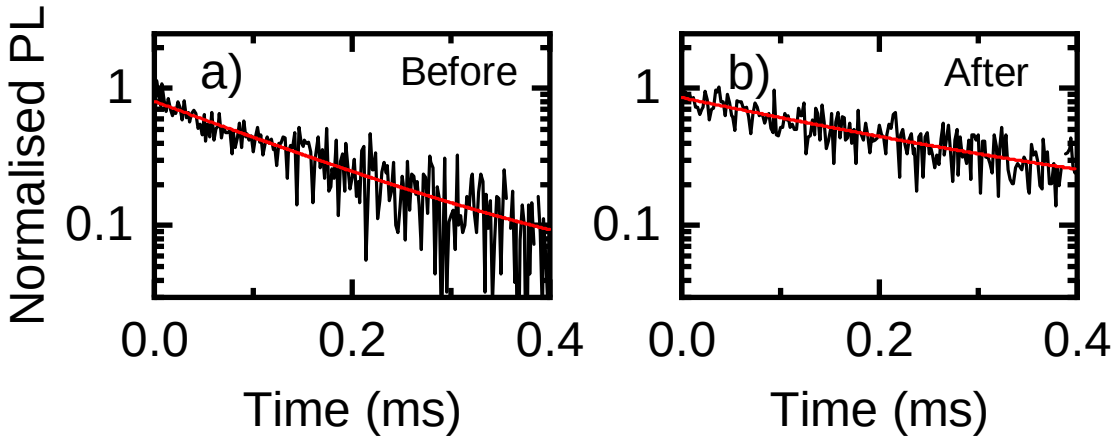

Supplementary Figure S18. **Effect of thermal cycling on the lifetime of delocalised interlayer excitons**. **(a)** Lifetime of delocalised interlayer excitons before the additional warm-up, cool-down cycle. The fit decay time from the exponential is τ=180 µs. **(b)** Lifetime measurement of delocalised interlayer excitons after the additional warm-up, cool-down cycle. The fit decay time from the exponential is τ=330 µs.

We test the robustness of the interlayer exciton emission peaks and lifetimes after one additional thermal cycle. After cooling device A to 4 K (stage 1), we warm it up at a rate of 1 K per minute until 70 K, and then at a rate of ∼0.3 K per minute until room temperature, while keeping the device in a He atmosphere at a room-temperature pressure of 17 mbar. A second cool-down is done at a rate of ∼0.5 K per minute from room temperature to 4 K (stage 2), while keeping the device in a He atmosphere at a room-temperature pressure of 17 mbar.

Supplementary Figure S17a and b are the spectra belonging to the same nanopillar site at stages 1 and 2, i.e. before and after one full warm-up, cool-down cycle, respectively. Comparison between spectra shows that some emission peaks remain unchanged (emission peaks 1-6 in Supplementary Figs. S17a,b). Nonetheless, there is a modification in the number of confined interlayer exciton emission peaks. Supplementary Figures S17c,d show the lifetimes of this nanopillar site before and after the thermal cycle, respectively. The lifetimes remain roughly the same: in both cases the biexponential fit is approximately τ_s=45 ns and τ_l=430 ns.

Supplementary Figure S18c,d show the lifetimes of the delocalised interlayer excitons before and after the thermal cycle, respectively. The lifetime is enhanced from 180 µs to 330 µs, possibly due to a slight modification in the interlayer distance after one thermal cycle.

We conclude that WS_2/WSe_2 heterostructures are sensitive to thermal cycling even when

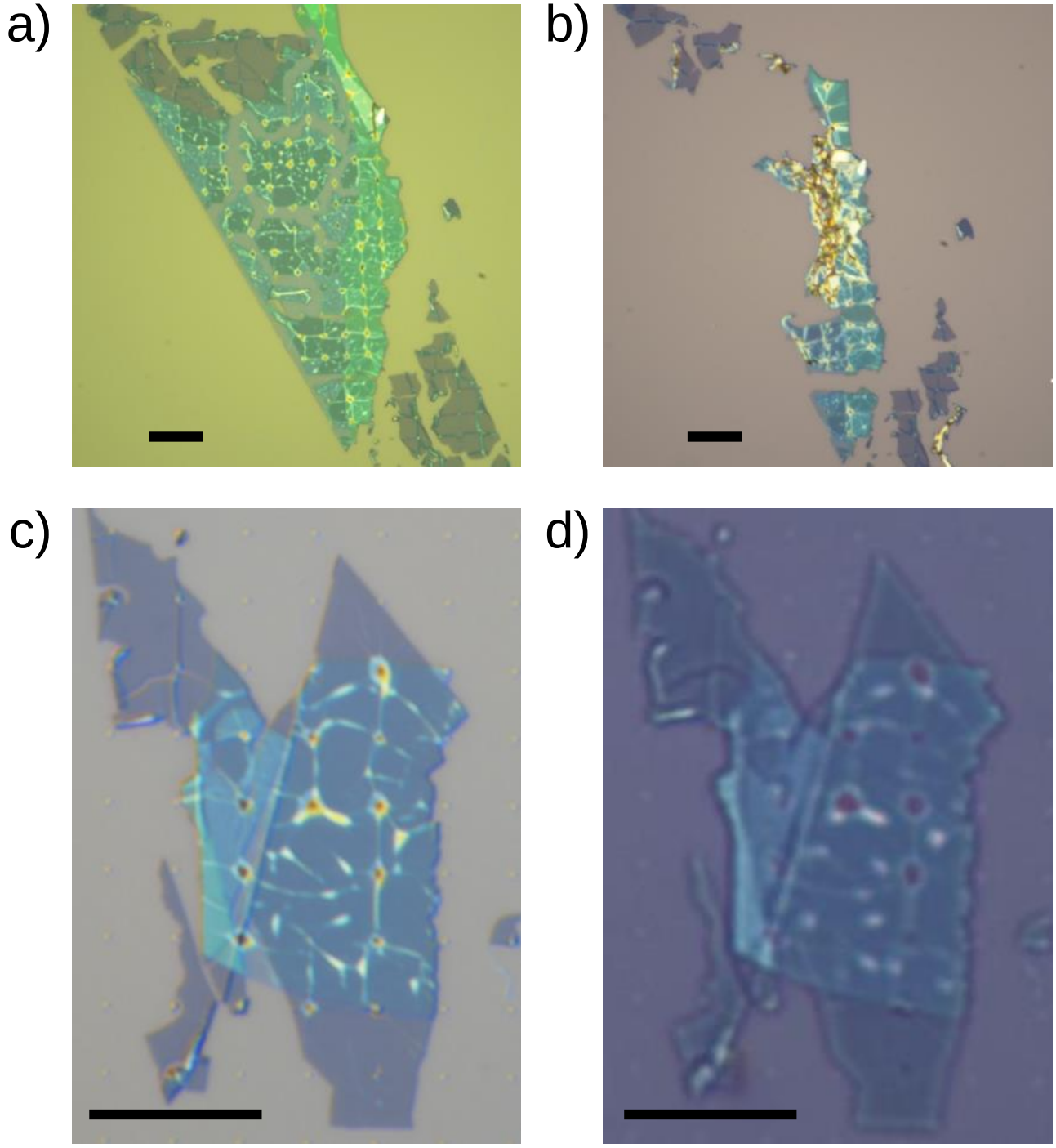

Supplementary Figure S19. **Effect of thermal cycling on the structural integrity of the devices**. **(a)** Optical image of WS_2/WSe_2 heterostructure on a nanopillar substrate before rapid warm-up. **(b)** Optical image of the same device as panel a, after a rapid warm-up in tens of minutes from 4 K to room temperature. **(c)** Optical image of device A before any thermal cycle. **(d)** Optical image of device A after two cool-down, warm-up cycles. Scale bars: 10 µm.

done very slowly, especially in the strained areas. That said, the overall properties of localised

interlayer emission and long lifetimes are retained.

We then subjected a second heterostructure to a rapid warm up of tens of minutes from 4 K to room temperature. Supplementary Figures S19a,b are the optical images of the second device before and after the rapid warm-up, respectively. The monolayers after this rapid warm-up roll up, rendering most of its area useless for subsequent studies. This is likely due to the accumulated strain being rapidly released. Supplementary Figures S19c,d are optical images of device A before and after a slow thermal cycle as described above. Supplementary Figs. S19c,d show that in this case the heterostructure retains its structural integrity.

Supplementary References

[1] Klug, H. P. *et al.* X-Ray Diffraction Procedures for Polycrystalline and Amorphous Materials, Second edition, John Wiley and Sons (1974).

[2] Spence, J. C. H. High-Resolution Electron Microscopy, Fourth Edition, Oxford University Press (2017).

[3] Barbone, M. *et al.* Charge-tuneable biexciton complexes in monolayer WSe_2. *Nat. Commun.* **9** 3721 (2018).

[4] Chernikov, A. *et al.* Electrical tuning of Exciton Binding Energies in Monolayer WS_2. *Phys. Rev. Lett.* **115**, 126802 (2015).

[5] Stier, A. V. *et al.* Probing the Influence of Dielectric Environment on Excitons in Monolayer WSe_2: Insight from High Magnetic Fields. *Nano Lett.* **16**, 7054-7060 (2016).

[6] Raja, A. *et al.* Dielectric disorder in two-dimensional materials. *Nat. Nanotechnol.* **14**, 832-837 (2019).

[7] Aslan, O. B. *et al.* Strain tuning of excitons in monolayer WSe_2. *Phys. Rev. B* **98**, 115308 (2018).

[8] Li, Z. *et al.* Efficient strain modulation of 2D materials via polymer encapsulation. *Nat. Commun.* **11** 1151 (2020).

[9] Buscema, M. *et al.* The effect of the substrate on the Raman and photoluminescence emission of single-layer MoS_2. *Nano Res.* **7**, 561-571 (2014).

[10] Lippert, S. *et al.* Influence of the substrate material on the optical properties of tunsgten diselenide monolayers. *2D Mater.* **4**, 025045 (2017).

[11] Cadiz, F. *et al.* Excitonic Linewidth Approaching the Homogeneous Limit in MoS_2-Based van der Waals Heterostructures. *Phys. Rev. X* **7**, 021026 (2017).

[12] Bozheyev, F. *et al.* Highly (001)-textured p-type WSe_2 Thin Films as Efficient Large-Area Photocathodes for Solar Hydrogen Evolution. *Sci. Rep.* **7**, 16003 (2017).

[13] Nakano, M. *et al.* Layer-by-layer Epitaxial Growth of Scalable WSe_2 on Sapphire by Molecular Beam Epitaxy. *Nano Lett.* **17**, 5595-5599 (2017).

[14] Edelberg, D. *et al.* Approaching the Intrinsic Limit in Transition Metal Diselenides via Point Defect Control. *Nano Lett.* **19**, 4371-4379 (2019).

[15] Terrones, H. *et al.* New first order Raman-active modes in few layered transition metal dichalcogenides. *Sci. Rep.* **4**, 4215 (2014).

[16] Zhao, W. *et al.* Lattice dynamics in mono- and few-layer sheets of WS_2 and WSe_2. *Nanoscale* **5**, 9677-9683 (2013).

[17] Lee, C. *et al.* Unveiling Defect-Related Raman Mode of Monolayer WS_2 via Tip-Enhanced Resonance Raman Scattering. *ACS Nano* **12**, 9982-9990 (2018).

[18] Hsu, W.-T. *et al.* Second Harmonic Generation from Artificially Stacked Transition Metal Dichalcogenide Twisted Bilayers. *ACS Nano* **8**, 2951-2958 (2014).

[19] Iff, O. *et al.* Strain-Tunable Single Photon Sources in WSe_2 Monolayers. *Nano Lett.* **19**, 6931-6936 (2019).

[20] Chakraborty, C. *et al.* Strain tuning of the emission axis of quantum emitters in an atomically thin semiconductor. *Optica* **7**, 580-585 (2020).

[21] Moon, H. *et al.* Strain-Correlated Exciton Energy in Atomically Thin Semiconductors. *ACS Photonics* **7**, 1135-1140 (2020).

[22] Palacios-Berraquero, C. *et al.* Large-scale quantum-emitter arrays in atomically thin semiconductors. *Nat. Commun.* **8**, 15093 (2017).

[23] Rosenberger, M *et al.* Nano-"Squeegee" for the Creation of Clean 2D Material Interfaces. *ACS Appl. Mater. Interfaces* **10**, 10379-10387 (2018).

[24] Rivera, P. *et al.* Observation of long-lived interlayer excitons in monolayer $MoSe_2$-WSe_2 heterostructures. *Nat. Commun.* **6**, 6242 (2015).

[25] Kremser, M. *et al.* Discrete interactions between a few interlayer excitons trapped at a $MoSe_2$-WSe_2 heterointerface. *NPJ 2D Mater. Appl.* **4**, 8 (2020).

[26] Nagler, P. *et al.* Interlayer exciton dynamics in a dichalcogenide monolayer heterostructure.

2D Mater. **4**, 025112 (2017).

[27] Yu, H. *et al.* Anomalous Light Cones and Valley Optical Selection Rules of Interlayer Excitons in Twisted Heterobilayers. *Phys. Rev. Lett.* **115**, 187002 (2015).

[28] Forg, M. *et al.* Cavity-control of interlayer excitons in van der Waals heterostructures. *Nat. Commun.* **10**, 3697 (2019).

[29] Li, W. *et al.* Dipolar interactions between localized interlayer excitons in van der Waals heterostructures. *Nat. Mater.* **19**, 624-629 (2020).

[30] Aivazian, G. *et al.* Magnetic control of valley pseudospin in monolayer WSe_2. *Nat. Phys.* **11**, 148-152 (2015).

[31] Shotan, Z. *et al.* Photoinduced Modification of Single-Photon Emitters in Hexagonal Boron Nitride. *ACS Photon.* **3**, 2490-2496 (2016).

[32] Tran, T. T. *et al.* Suppression of spectral diffusion by anti-Stokes Excitation of quantum emitters in hexagonal boron nitride. *Appl. Phys. Lett.* **115**, 071102 (2019).

[33] Branny, A. *et al.* Deterministic strain-induced arrays of quantum emitters in a two-dimensional semiconductor. *Nat. Commun.* **8**, 15053 (2017).

[34] Tighineanu, P. *et al.* Decay dynamics and exciton localization in large GaAs quantum dots grown by droplet epitaxy. *Phys. Rev. B* **88**, 155320 (2013).

[35] Berciaud, S. *et al.* Luminescence Decay and the Absorption Cross Section of Individual Single-Walled Carbon Nanotubes. *Phys. Rev. Lett.* **101**, 077402 (2008).

[36] Wozniak, T. *et al.* Exciton g factors of van der Waals heterostructures from first-principles calculations. *Phys. Rev. B* **101**, 235408 (2020).

[37] Deilmann, T. *et al.* Ab initio Studies of Exciton g Factors: Monolayer Transition Metal Dichalcogenides in Magnetic Fields. *Phys. Rev. Lett.* **124**, 226402 (2020).

[38] Jahnke, K. D. *et al.* Electron–phonon processes of the silicon-vacancy centre in diamond. *New J. Phys.* **17**, 043011 (2015).

[39] Toyli, D. M. *et al.* Measurement and Control of Single Nitrogen-Vacancy Center Spins above 600 K. *Phys. Rev. X* **2**, 031001 (2012).